





## Magnetic structure and magnetoelectric coupling in the antiferromagnet $\text{Co}_5(\text{TeO}_3)_4\text{Cl}_2$

B. Yu <sup>1</sup>, L. Huang,<sup>1</sup> J. S. Li,<sup>2</sup> L. Lin ,<sup>2,1,\*</sup> V. Ovidiu Garlea <sup>3</sup>, Q. Zhang <sup>3</sup>, T. Zou,<sup>4</sup> J. C. Zhang,<sup>5</sup> J. Peng,<sup>5</sup> Y. S. Tang,<sup>6</sup> G. Z. Zhou,<sup>1</sup> J. H. Zhang,<sup>1</sup> S. H. Zheng,<sup>7</sup> M. F. Liu,<sup>7</sup> Z. B. Yan,<sup>1</sup> X. H. Zhou,<sup>1</sup> S. Dong,<sup>5</sup> J. G. Wan,<sup>1,†</sup> and J.-M. Liu<sup>1</sup>

<sup>1</sup>Laboratory of Solid State Microstructures, Nanjing University, Nanjing 210093, China

<sup>2</sup>Department of Applied Physics, College of Science, Nanjing Forestry University, Nanjing 210037, China

<sup>3</sup>Neutron Science Division, Oak Ridge National Laboratory, Oak Ridge, Tennessee 37831, USA

<sup>4</sup>Collaborative Innovation Center of Light Manipulations and Applications, Shandong Normal University, Jinan 250358, China

<sup>5</sup>Key Laboratory of Quantum Materials and Devices of Ministry of Education, School of Physics, Southeast University, Nanjing 211189, China

<sup>6</sup>School of Science, Nanjing University of Posts and Telecommunications, Nanjing 210023, China

<sup>7</sup>Institute for Advanced Materials, Hubei Normal University, Huangshi 435002, China



(Received 4 January 2024; accepted 18 April 2024; published 6 May 2024)

The van der Waals (vdW) layered multiferroics, which host simultaneous ferroelectric and magnetic orders, have attracted attention not only for their potentials to be utilized in nanoelectric devices and spintronics, but also offer alternative opportunities for emergent physical phenomena. To date, the vdW layered multiferroic materials are still very rare. In this work, we have investigated the magnetic structure and magnetoelectric (ME) effects in  $\text{Co}_5(\text{TeO}_3)_4\text{Cl}_2$ , a promising multiferroic compound with antiferromagnetic (AFM) Néel point  $T_N \sim 18$  K. The neutron-powder diffraction reveals the noncoplanar AFM state with preferred Néel vector along the  $c$  axis, while a spin reorientation occurring between 8 and 15 K is identified, which results from the distinct temperature dependence of the nonequivalent Co site's moment in  $\text{Co}_5(\text{TeO}_3)_4\text{Cl}_2$ . Moreover, it is found that  $\text{Co}_5(\text{TeO}_3)_4\text{Cl}_2$  is one of the best vdW multiferroics studied so far in terms of the multiferroic performance. The measured linear ME coefficient exhibits the emergent oscillation dependence of the angle between magnetic field and electric field, and the maximal value is as big as 45 ps/m. It is suggested that  $\text{Co}_5(\text{TeO}_3)_4\text{Cl}_2$  is an appreciated platform for exploring the emergent multiferroicity in vdW layered compounds.

DOI: [10.1103/PhysRevB.109.184106](https://doi.org/10.1103/PhysRevB.109.184106)

### I. INTRODUCTION

Multiferroic materials, which simultaneously possess more than one ferroic order, have attracted attention due to their intriguing physical phenomena and potential applications [1–3]. In particular, the cross coupling between magnetic and electric orders allows a control of magnetization ( $M$ ) by electric field ( $E$ ) or electric polarization ( $P$ ) by magnetic field ( $H$ ) [4–6]. However, most of the observed spin order-induced ferroelectricity effects occur at low temperature ( $T$ ) or the magnetoelectric (ME) coupling is more or less weak [7,8], leaving linear ME materials opportunity to be further explored, such as the time-honored  $\text{Cr}_2\text{O}_3$  [9–11]. Based on the symmetry requirement, these linear ME compounds usually exhibit collinear spin order with nonpolar magnetic point group and nonferroelectricity. The magnetically induced ferroelectricity can only be triggered by magnetic field ( $H$ ).

It is noted that linear ME effect does not necessarily require a highly frustrated structure and may be allowed even in nonpolar crystals [10,12,13], offering many more opportunities for finding linear ME compounds including two-dimensional (2D) materials. Indeed, a set of emergent ferroic phenomena has been unveiled in recent years in 2D van der Waals (vdW)

family of materials such as ferroelectricity in  $\text{CuInP}_2\text{S}_6$  [14] and  $\text{In}_2\text{Se}_3$  [15,16], magnetism in  $\text{Cr}_2\text{Ge}_2\text{Te}_6$  [17] and  $\text{CrI}_3$  [18,19], etc. Although  $\text{CuCrP}_2\text{S}_6$  [20–22] and  $\text{NiI}_2$  were reported to exhibit comparatively ME effect [23–26], 2D vdW multiferroics are yet rare. In such sense, searching for 2D vdW multiferroic compounds seems to be a cutting-edge topic these years.

Recently, vdW magnets  $A_5(\text{TeO}_3)_4X_2$  ( $A = \text{Ni}, \text{Co}$ ; and  $X = \text{Cl}, \text{Br}, \text{I}$ ) in monoclinic structure with space group  $C2/c$  have been receiving attention for their attractive magnetic structures and lattice symmetry variants. The crystal structure of this family consists of three unequal  $A$  octahedra [ $A(1)\text{O}_6$ ], [ $A(2)\text{O}_5X$ ], and [ $A(3)\text{O}_6$ ], forming a clamplike corner-shared [ $A_5\text{O}_{17}X_2$ ] unit [27,28]. Each layers consists of two clamplike [ $A_5\text{O}_{17}X_2$ ] units with center of inversion symmetry are stacked along the  $a$  axis through vdW interaction to form a layered structure. As revealed by neutron diffraction on  $\text{Ni}_5(\text{TeO}_3)_4\text{Br}_2$  in Ref. [29], the three inequivalent  $A$  octahedra have different magnetic moments due to their different distortion degrees and crystal fields. Consequently, a noncollinear spin arrangement in the  $ac$  plane below the Néel temperature  $T_N = 29$  K is established, resulting in a  $C2'/c$  magnetic space group. Based on symmetry analysis, a  $C2'/c$  magnetic space group allows linear ME coupling, thus making  $A_5(\text{TeO}_3)_4X_2$  family potentially another class of multiferroics. Along this line, a success in observing the linear ME effect in  $A_4B_2\text{O}_9$  ( $A = \text{Mn}, \text{Fe}, \text{Co}, \text{Ni}$ ; and  $B = \text{Nb}, \text{Ta}$ ) compounds

\*llin@njfu.edu.cn

†wanjg@nju.edu.cn

stimulates us to further explore those isostructural counterparts in  $A_5(\text{TeO}_3)_4X_2$  family, noting that the spin-orbit coupling (SOC) plays a significant role in the origin of magnetically induced electric polarization [30–32]. Among the  $A_5(\text{TeO}_3)_4X_2$  family, Co-based materials with  $3d^7$  ( $S = 3/2$ ) magnetic cations possess stronger anisotropy and SOC effect [28]. To the best of our knowledge, the magnetic structures and ME coupling effects of  $\text{Co}_5(\text{TeO}_3)_4X_2$  ( $X = \text{Cl, Br, I}$ ) have not been well studied yet, deserving further investigation.

Here, we experimentally demonstrate a large magnetic control of electric polarization in vdW magnet  $\text{Co}_5(\text{TeO}_3)_4\text{Cl}_2$  ceramic sample and single crystal by a series of characterizations on structure, magnetic susceptibility, and ME response. Unlike the Ni-based compounds where the spins are confined within the  $ac$  plane, our powder neutron-scattering data show the noncoplanar antiferromagnetic (AFM) order with Néel vector aligned along the  $c$  axis. Furthermore, it is demonstrated that the samples exhibit larger magnetically induced electric polarization and stronger ME coupling in comparison with the currently known van der Waals layered magnetoelectric materials, suggesting that  $\text{Co}_5(\text{TeO}_3)_4\text{Cl}_2$  would be a more promising vdW multiferroic and a preferred platform for exploring 2D multiferroicity.

## II. EXPERIMENTAL DETAILS

Polycrystalline samples of  $\text{Co}_5(\text{TeO}_3)_4\text{Cl}_2$  were prepared using conventional solid-state reaction method [28]. Stoichiometric mixture of high-purity  $\text{CoO}$ ,  $\text{CoCl}_2$ , and  $\text{TeO}_2$  was thoroughly ground, and placed in evacuated silica ampoules, and sintered at  $570^\circ\text{C}$  for 72 h in a muffle furnace. To ensure the sample purity, the aforementioned process was repeated three times. Then, the pure-phase powder was thoroughly reground and pressed into a rod under a hydrostatic pressure. The rodlike sample was sintered at  $570^\circ\text{C}$  for 72 h and cut into disks  $\sim 0.4$  mm in thickness for subsequent electrical measurements. The single crystals were grown by chemical vapor transport technique with polycrystalline powder and  $\text{TeCl}_4$  as transport agent as described in Ref. [28]. The samples were characterized by the x-ray diffraction (XRD, D8 Advanced, Bruker) in the  $\theta$ - $2\theta$  mode with  $\text{Cu K}\alpha$  source ( $\lambda = 1.5406 \text{ \AA}$ ) at room temperature. To verify the stoichiometry of samples, the chemical composition was analyzed using electron dispersion spectroscopy (EDS) with an FEI Quanta 200 scanning electron microscope (SEM). Additionally, the morphology of samples was examined using SEM to highlight the preferred orientation.

The magnetic susceptibility ( $\chi$ ) as a function of  $T$  from 2 to 300 K was measured using the Quantum Design Superconducting Quantum Interference Device magnetometer (SQUID) in both the zero-field-cooled (ZFC) and field-cooled (FC) modes, with measuring field  $\mu_0H = 1$  kOe. The  $H$ -dependent magnetization  $M$  was measured at selected  $T$  using the vibrating sample magnetometer in the Physical Property Measurement System (PPMS, Quantum Design). The specific heat ( $C_P$ ) was measured using the PPMS in the standard procedure.

Neutron-powder diffraction was conducted at powder diffractometer (POWGEN) located at the Spallation Neutron

Source, Oak Ridge National Laboratory. The POWGEN automatic sample changer was selected as the sample environment to cover the  $T$  range from 10 to 300 K. The powder sample was loaded in a standard vanadium can and sealed with the helium exchange gas. The neutron bank with center wavelength  $2.665 \text{ \AA}$  was used to collect the neutron data covering  $d$  spacing from 1 to  $21 \text{ \AA}$ . Magnetic structure was determined by the Rietveld analysis on the POWGEN data using GSAS-II software [33].

To measure ferroelectric properties, a sandwich-type capacitor was fabricated by depositing a layer of Au on both the top and bottom surfaces of a sample with a diameter of 5.0 mm and a thickness of  $\sim 0.4$  mm. The pyroelectric current was measured from 2 to 30 K with a  $T$ -ramp rate of 4 K/min using a Keithley 6514 electrometer. To ensure a single-domain state, the ME poling procedure was applied. In detail, the sample was poled under an electric field of 3.33 kV/cm and selected magnetic field over  $T$  range from 50 to 2 K. Then, the poling electric field was removed before measuring the pyroelectric current. To investigate the ME effect, the  $H$ -dependent ME current ( $I_{\text{ME}}$ ) was measured under selected  $T$  upon  $\mu_0H$  ramping from  $+9$  to  $-9$  T at a rate of 100 Oe/s using the same ME poling procedure. Finally, the  $T$  and  $H$  dependences of electric polarization  $P$  were obtained by integrating of the pyroelectric current or magnetoelectric current with time. For the ME measurements of single crystal, the sample was applied under the same ME poling procedure in the  $E//a^*$  axis and  $H$  parallel to  $a^*$ ,  $b$ , and  $c$  axes, whereas  $a^* \perp bc$  plane.

## III. RESULTS AND DISCUSSION

### A. Crystal structure

As mentioned,  $\text{Co}_5(\text{TeO}_3)_4\text{Cl}_2$  belongs to monoclinic structure with space group  $C2/c$  and is isomorphic to  $\text{Ni}_5(\text{TeO}_3)_4\text{Cl}_2$ . Figure 1(a) illustrates how  $\text{Co}_5(\text{TeO}_3)_4\text{Cl}_2$  units are stacked along the  $a$  axis through interlaminar vdW interactions: three unequal Co octahedra [ $\text{Co}(1)\text{O}_6$ ], [ $\text{Co}(2)\text{O}_5\text{Cl}$ ], and [ $\text{Co}(3)\text{O}_6$ ], whereas symbols  $\text{Co}_1$ ,  $\text{Co}_2$ , and  $\text{Co}_3$  denote the different Co occupations forming a clamplike Cobalt pentamer cluster of [ $\text{Co}_5\text{O}_{17}\text{Cl}_2$ ] units. In Fig. 1(b) we present the slow-scan XRD pattern of the ceramic sample. The robust orientation preference is observed, evidenced by the strong intensity of the pronounced sharp ( $h00$ ) peaks, e.g., (200), (400), and (800), while the peaks in other orientations appear considerably weaker. Further Rietveld refinement is performed on the fully ground crushed ceramics [28]. It shows that all the reflection peaks can be well fitted by standard database for  $C2/c$  monoclinic lattice and no impurity phase is detected. The refined structural parameters are  $a = 19.729(2) \text{ \AA}$ ,  $b = 5.264(8) \text{ \AA}$ ,  $c = 16.437(1) \text{ \AA}$ ,  $\alpha = \gamma = 90^\circ$ , and  $\beta = 125.25(9)^\circ$ , consistent with Ref. [28]. To check more details of the grains and crystal orientation, we performed SEM image of the ceramic sample as shown in Fig. 1(c), which exhibits a prominent flake shape suggesting a strong orientation preference. Furthermore, a few inclined and vertical sheets can be observed, contributing to the strong intensity of XRD pattern. The analysis of sample chemical composition using EDS reveals an atomic ratio of Co:Te:Cl

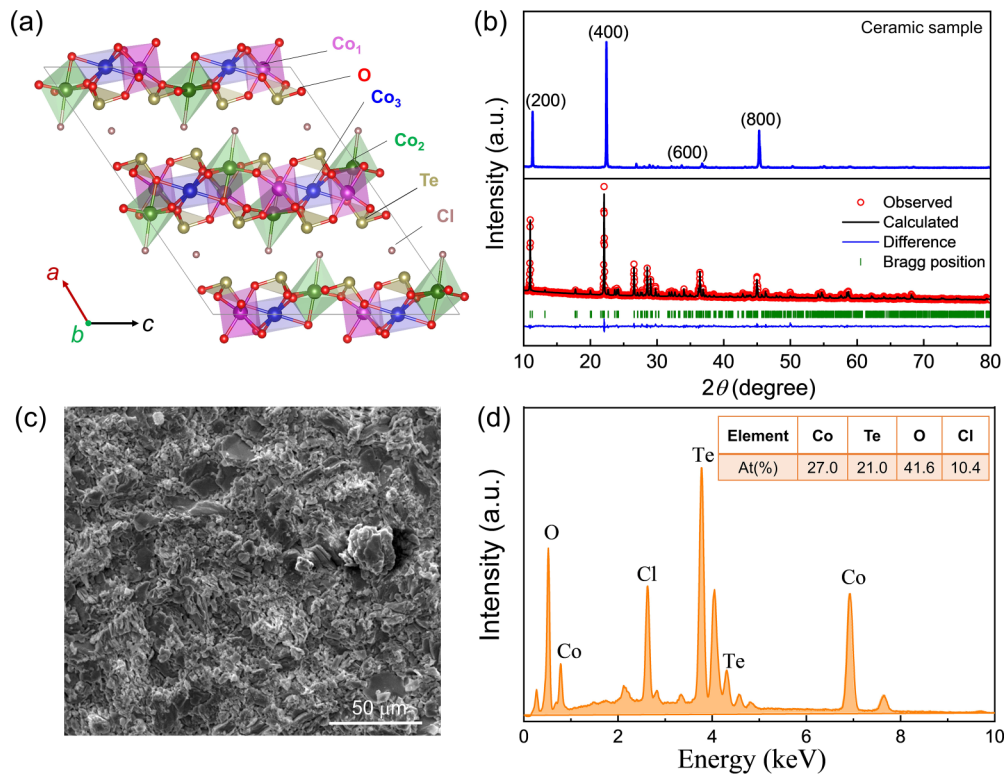


FIG. 1. (a) The crystal structure of  $\text{Co}_5(\text{TeO}_3)_4\text{Cl}_2$  viewed along the [010] direction. Three cobalt-oxygen (red spheres) cages are illustrated in the magenta, green, and blue, respectively. (b) The XRD of ceramic sample and the refined XRD pattern of the crushed ceramics collected at room temperature. (c) Micromorphology of ceramic samples under SEM and (d) EDS spectra.

as 5.19:4.03:2, which is consistent with the expected stoichiometric ratio of  $\text{Co}_5(\text{TeO}_3)_4\text{Cl}_2$ , as shown in Fig. 1(d).

### B. Magnetic properties and specific heat

Figure 2(a) depicts the  $T$  dependence of magnetic susceptibility ( $\chi$ ) in the ZFC and FC conditions. The overlapping ZFC and FC curves both show a sharp peak at  $T = T_N \sim 18$  K, the AFM Néel point. The Curie-Weiss fitting of the data from 100 to 300 K gives rise to Curie-Weiss temperature  $\theta_{\text{CW}} \sim -68$  K, indicating the AFM nature of the  $\text{Co}^{2+}$  spin exchange. The derived effective paramagnetic moment  $\mu_{\text{eff}} \sim 5.2\mu_{\text{B}}/\text{Co}^{2+}$  falls in the expected spin-only moment  $3.87\mu_{\text{B}}/\text{Co}$  and total effective moment  $6.64\mu_{\text{B}}/\text{Co}$ , revealing the contribution from the orbital angular momentum via the spin-orbit coupling. In addition, the frustration factor  $f = |\theta_{\text{CW}}/T_N|$  is  $\sim 3.8$ , implying a weak frustration. The measured isothermal  $M$ - $H$  dependences at different  $T$  show no evident field-induced metamagnetic transition up to  $\mu_0 H \sim 9$  T as shown in Fig. 2(b).

The AFM ordering at  $T_N$  can be further confirmed by the heat-capacity data, as shown in Fig. 2(c), exhibiting the typical  $\lambda$ -like anomaly at  $T_N$ . While the standard Debye model is used to evaluate the phonon contribution  $C_{\text{latt}}$ , a subtraction of this term allows the magnetic contribution  $C_M$  to be obtained, as shown by the blue line in Fig. 2(c). The magnetic entropy  $\Delta S_M$  estimated by integrating  $C_M/T$  over the whole  $T$  range, presented by the blue line in Fig. 2(d), shows a value of  $\sim 37$  J mol $^{-1}$  K $^{-1}$  of magnetic entropy, about 60% of the total value  $5R \ln(2J + 1) = 57.6$  J mol $^{-1}$  K $^{-1}$ , indicating the  $\text{Co}^{2+}$  angular momentum  $J = 3/2$ .

### C. Neutron-powder diffraction

To unveil the spin configuration with the AFM state, we discuss the neutron-powder diffraction (NPD) data shown in Fig. 3, collected at  $T = 30$ , 15, and 8 K, respectively. The Rietveld refinement confirms the space group  $C2/c$ . At  $T = 30$  K, the refined lattice constants are  $a = 19.557(7)\text{\AA}$ ,  $b = 5.259(3)\text{\AA}$ , and  $c = 16.366(4)\text{\AA}$ , consistent with the XRD data; details are listed in Table I. It is noted that additional Bragg peaks, e.g.,  $Q \sim 0.47$  and  $0.64\text{\AA}^{-1}$ , appear below  $T_N$ , due to the magnetic scattering. By subtracting the paramagnetic nuclear contribution ( $T = 30$  K) from the data obtained at  $T = 15$  and 8 K, the pure magnetic contribution was isolated, as shown in the insets of Figs. 3(b) and 3(c). The clear magnetic reflections denoted by (001), (20-1), and (20-3) are well explained by the wave-propagation vector  $\mathbf{k} = (0, 0, 0)$ .

To gain deeper insights into the magnetic structure, it is instructive to map out the magnetic Co sublattices. Figure 4(a) shows the three unequal Co octahedra [ $\text{Co}(1)\text{O}_6$ ], [ $\text{Co}(2)\text{O}_5\text{Cl}$ ], and [ $\text{Co}(3)\text{O}_6$ ], whereas symbols  $\text{Co}_1$ ,  $\text{Co}_2$ , and  $\text{Co}_3$  denote the different Co sites forming a clamplike cobalt pentamer cluster of [ $\text{Co}_5\text{O}_{17}\text{Cl}_2$ ] units at  $T > T_N$ . These clusters consist of five Co octahedra, denoted as  $\text{Co}_1$ ,  $\text{Co}'_1$ ,  $\text{Co}_2$ ,  $\text{Co}'_2$ , and  $\text{Co}_3$ , as illustrated in Figs. 4(b) to 4(e). The arrangement of the three nonequivalent Co sites is reminiscent of the magnetically frustrated bowtie lattice consisting of vertex-sharing triangles.

Based on the symmetry analysis using the tools at Bilbao Crystallographic Server [34], the irreducible representation  $m\text{GM}2$ -corresponding to the magnetic space group  $C2'/c$ ,

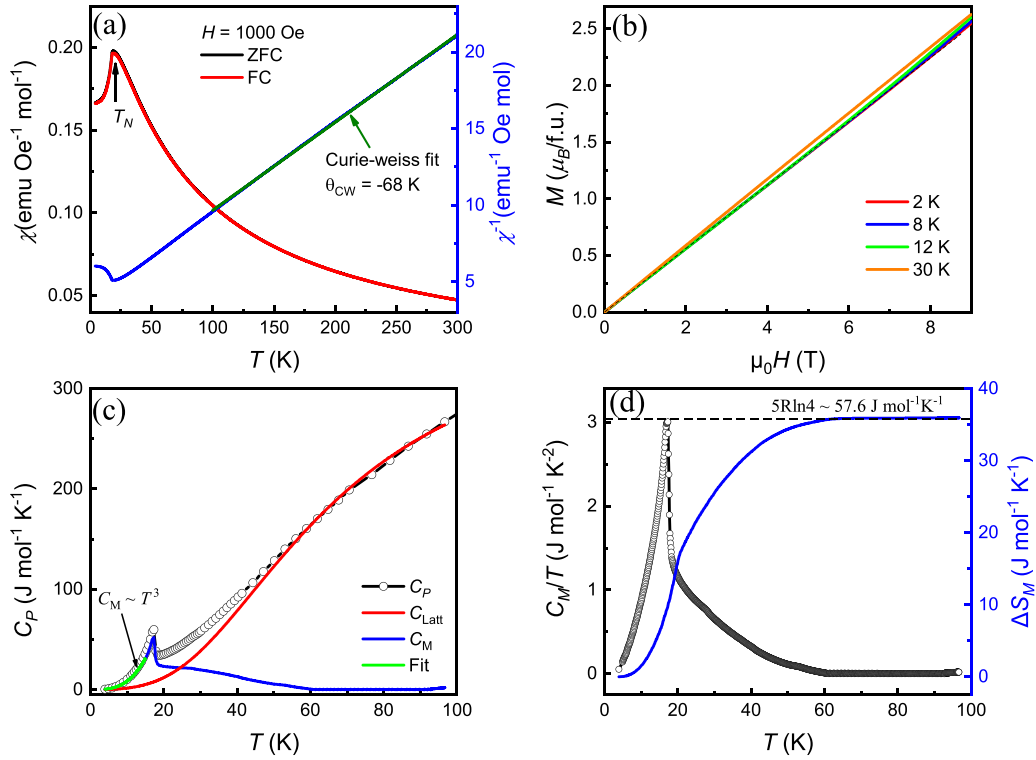


FIG. 2. (a) The  $T$  dependence of the magnetic susceptibility of  $\text{Co}_5(\text{TeO}_3)_4\text{Cl}_2$  under ZFC and FC modes with measuring field  $\mu_0 H = 1$  kOe. The right axis shows the  $T$ -dependent inverse susceptibility. (b) Depiction of the isothermal magnetization as a function of  $H$  at different temperatures from 2 to 30 K. (c) Heat capacity vs temperature curve measured from  $T = 4$  to 100 K. The red line and the blue line represent the lattice contribution ( $C_{\text{latt}}$ ) and the magnetic contribution ( $C_M$ ), respectively. (d) The  $C_M/T$  (left axis) and magnetic entropy ( $\Delta S_M$ ) (right axis) as a function of temperature.

yields the closest agreement with the experimental data. The magnetic point group is  $2'/m$  below  $T_N$ , which forbids spontaneous polarization but allows the linear ME effect. The magnetic moments of  $\text{Co}_1$  and  $\text{Co}_2$  positions are allowed to point in any direction of the lattice, while the  $\text{Co}_3$  moment is constrained to lie in the  $ac$  plane. The refined values for  $\text{Co}^{2+}$  moments at each site and at  $T = 15$  and 8 K are given in Table II. It is found that the  $\text{Co}_3$  ion situated at the center bowtie has a much smaller ordered moment, which indicates a strong site-dependent magnetic frustration, similar to the observations for similar bowtie system  $\text{Ca}_2\text{Mn}_3\text{O}_8$  [35] and  $\text{Mn}_5(\text{VO}_4)_2(\text{OH})_4$  [36]. The  $\text{Co}^{2+}$  moments form a noncoplanar structure, in which the nearest  $\text{Co}_1$  and  $\text{Co}_2$  moments tend to align in the same direction, but opposite to the  $\text{Co}_3$  moment.

In addition, a comparison of the magnetic arrangements refined at 15 and 8 K confirms that the temperature dependence of the  $\text{Co}_3$  moment is different from those of  $\text{Co}_1$  and  $\text{Co}_2$ . The  $\text{Co}_3$  moment value increases more rapidly (77%) compared to the other two moment values (61% for  $\text{Co}_1$  and 57% for  $\text{Co}_2$ ). It is worth noting that the magnetic moment at different sites varies significantly along different directions. The  $\text{Co}_3$  moment value ( $M_z$ ) along the  $z$  direction has increased by 77%, while the  $\text{Co}_1$  and  $\text{Co}_2$  moment values ( $M_z$ ) have increased by 19 and 57%, respectively. The variation is just in accordance with a previous report in  $\text{Ni}_5(\text{TeO}_3)_4\text{Br}_2$  by Pregelj *et al.*, whereas the distinct temperature dependence of the nonequivalent Ni sites has been revealed [29]. In contrast to

$\text{Ni}_5(\text{TeO}_3)_4\text{Br}_2$ , where the moments are exclusively confined to the  $ac$  plane, the magnetic moments of  $\text{Co}_5(\text{TeO}_3)_4\text{Cl}_2$  are noncoplanar and include components along the  $b$  direction. In addition, the  $\text{Co}_2$  moment value ( $M_y$ ) along the  $y$  direction decreases by 34%, while the sign of  $\text{Co}_1$  moment  $M_y$  has changed from  $y$  direction to  $-y$  direction, indicative of the spin reorientation between 8 and 15 K.

#### D. Anisotropic ME effects

Herein, special attention is given to checking the potential ME coupling effect based on the magnetic structure. As the bulk sample shows strong preference orientation along the  $a^*$  axis, for comparison, the  $H$ -induced electric polarization  $P$  as a function of  $T$  was measured for  $H$  parallel ( $H_{\parallel}$ ) and perpendicular ( $H_{\perp}$ ) to the poling electric field  $E$ . Figures 5(a) and 5(b) depict the pyroelectric current ( $I$ ) and  $P$ , given of  $\text{Co}_5(\text{TeO}_3)_4\text{Cl}_2$  in a magnetic field of  $\mu_0 H_{\parallel} = 0$  and 9 T with different  $E$  settings. It is seen that  $P = 0$  at  $\mu_0 H_{\parallel} = 0$ , reasonable due to the centrosymmetric space group. However, the pyroelectric current  $I$  rises rapidly as  $T$  increases to  $T_N$ , and forms a broad peak at nonzero  $H$ . The measured  $P$  is also proportional to  $E$ , indicating incomplete polarized ME domains. Besides, the symmetrical  $I(E)$  shows that the polarization can be switched by reversing  $E$ . More examination of the ME effect is presented in Figs. 5(c) and 5(d), while a clear linear ME effect is seen below  $\mu_0 H = 7$  T, a deviation from

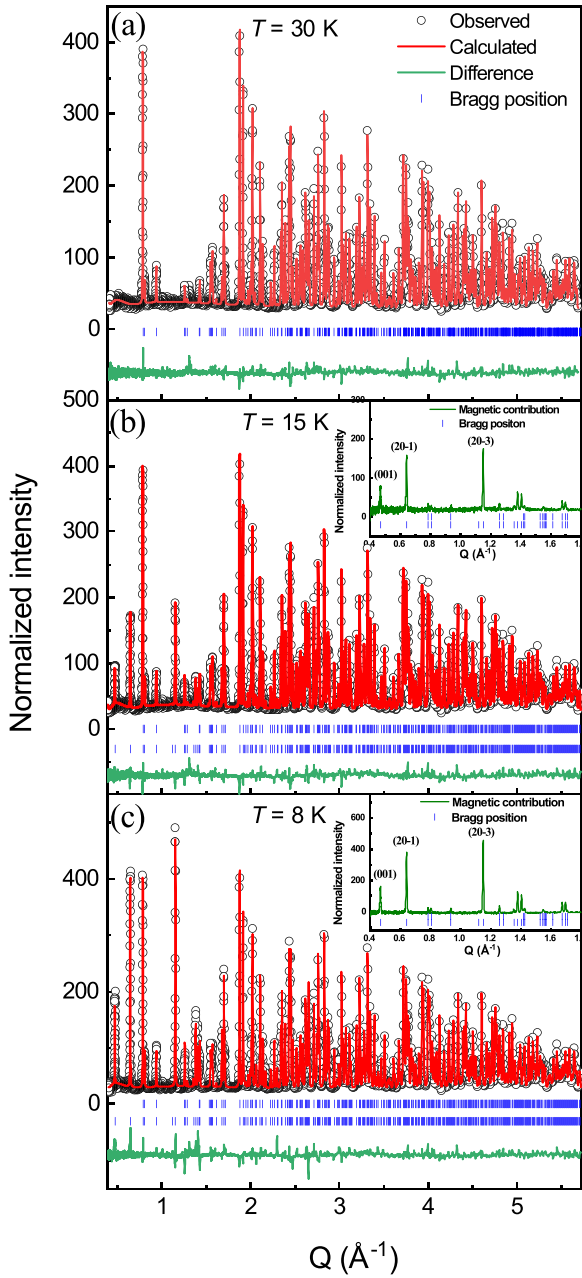


FIG. 3. Rietveld refinement plots of the NPD data at (a) 30 K, (b) 15 K, and (c) 8 K. The ticks below the graphs indicate the calculated Bragg position of the crystal structure (upper row) and magnetic structure (lower row) and magnetic structure at 15 and 8 K are shown in the inset.

the linear  $P(H)$  dependence, as seen in the inset of Fig. 5(d). Overall,  $P$  can be as large as  $\sim 160 \mu\text{C}/\text{m}^2$  at  $\mu_0 H_{\parallel} = 8 \text{ T}$  and  $T = 2 \text{ K}$ , an appreciated ME effect considering the polycrystalline nature of the samples. Nevertheless, as the bulk sample shows strong preference orientation, one is allowed to check the electric polarization in the perpendicular magnetic field. Figures 5(e) and 5(f) show the  $T$  dependence of  $I$  and  $P$  in various  $H_{\perp}$  configurations. It is seen that similar ME response of  $\text{Co}_5(\text{TeO}_3)_4\text{Cl}_2$  against  $H$  is obtained, as shown in the inset of Fig. 5(f). However, it should be noted that the intensity of polarization has doubled, indicating the

TABLE I. Structural parameters for  $\text{Co}_5(\text{TeO}_3)_4\text{Cl}_2$  refined from NPD data at 30 K. Space group:  $C2/c$ ,  $a = 19.557(7) \text{ \AA}$ ,  $b = 5.259(3) \text{ \AA}$ ,  $c = 16.366(4) \text{ \AA}$ ,  $\alpha = \gamma = 90^\circ$ , and  $\beta = 125.05(5)^\circ$ . GOF stands for Goodness of fitting.

Atom	Site	$x$	$y$	$z$	$U$
Co1	8 <i>f</i>	0.0081(7)	0.2196(4)	0.6169(4)	0.000 51
Co2	8 <i>f</i>	0.0925(3)	0.2167(5)	0.4754(0)	0.000 51
Co3	4 <i>e</i>	0	0.2389(2)	1/4	0.000 51
Te4	8 <i>f</i>	0.1287(5)	0.3130(4)	0.1407(4)	0.002 51
Te5	8 <i>f</i>	0.1491(8)	0.2936(1)	0.8782(9)	0.002 51
Cl6	8 <i>f</i>	0.2419(2)	0.3218(9)	0.5977(7)	0.002 70
O7	8 <i>f</i>	0.0415(4)	0.1626(1)	0.1429(1)	0.002 50
O8	8 <i>f</i>	0.0663(0)	0.4909(1)	0.3692(3)	0.002 50
O9	8 <i>f</i>	0.0721(2)	0.3893(4)	0.5690(6)	0.002 50
O10	8 <i>f</i>	0.0787(6)	0.0179(5)	0.8557(2)	0.002 50
O11	8 <i>f</i>	0.0986(1)	0.1434(0)	0.0228(0)	0.002 50
O12	8 <i>f</i>	0.1153(4)	0.3431(1)	0.7491(7)	0.002 50

$R_{\text{WP}} = 5.093$ ,  $\text{GOF} = 4.16$ .

presence of an anisotropic ME effect in our polycrystalline sample.

In order to further investigate its linear ME coupling effect, the  $H$  dependence of ME current ( $I_{\text{ME}}$ ) and field-induced polarization ( $\Delta P$ ) measured in the  $H//E$  configuration at different temperatures upon  $\mu_0 H$  ramping from  $+9 \text{ T} \sim -9 \text{ T} \sim +9 \text{ T}$  at a rate of  $100 \text{ Oe/s}$  are displayed in Figs. 6(a) and 6(b), respectively, whereas the green arrow indicates the scanning magnetic field direction. As the magnetic field scans from 9 to 0 T, there is a sharp increase of  $I_{\text{ME}}$  between 7.5 and 9 T, accompanied by slowly released current with the decrease of magnetic field. The current shape in the positive and negative magnetic field regions shows good symmetry. Figure 6(b) present the electric polarization  $\Delta P$  in the sweeping magnetic field, and the relationship between polarization and the magnetic field showcases a clear linear trend below 7 T with the coefficient  $a_{\parallel} = 18 \text{ ps/m}$ . It is noted that the ME response shows obvious deviation from linearity at high field, and the critical field is roughly consistent with that observed in the isofield experiments as shown in the inset of Fig. 5(f). Moreover, the ME response in the  $H \perp E$  configuration exhibits a similar linear trend, as shown Fig. 6(d). However, the linear ME coupling coefficient  $\alpha_{\perp}$  reaches an impressive magnitude of  $45 \text{ ps/m}$ , larger than  $a_{\parallel}$  and the currently known van der Waals layered ME materials, such as  $\text{MX}_2$  ( $M = \text{transition metal}$ ,  $X = \text{halogen}$ ) [37–41], and  $\text{CuCrP}_2\text{S}_6$  [20]. More details of the ME performance of some vdW ME materials are summarized in Table III.

To further illustrate the anisotropic ME effects, we performed the angular ( $\theta$ ) dependence of magnetically induced polarization  $\Delta P$  in rotating  $\mu_0 H = 7 \text{ T}$  at  $T = 2 \text{ K}$  after the ME poling procedure. Here, the angle  $\theta$  denotes the direction of magnetic field with respect to the direction of the normal vector on a sample surface, as shown in Fig. 7. Thus,  $\theta = 0$  and  $\theta = 90^\circ$  represent  $H//E$  and  $H \perp E$  configurations. The ME coupling coefficient in the parallel and vertical configurations is denoted as  $a_{\parallel}$  and  $\alpha_{\perp}$ , respectively. Due to the polycrystalline feature, the magnetically induced polarization  $\Delta P$  is proportional to  $\Delta P = \alpha_{\parallel} H_{\parallel} + \alpha_{\perp} H_{\perp}$ .

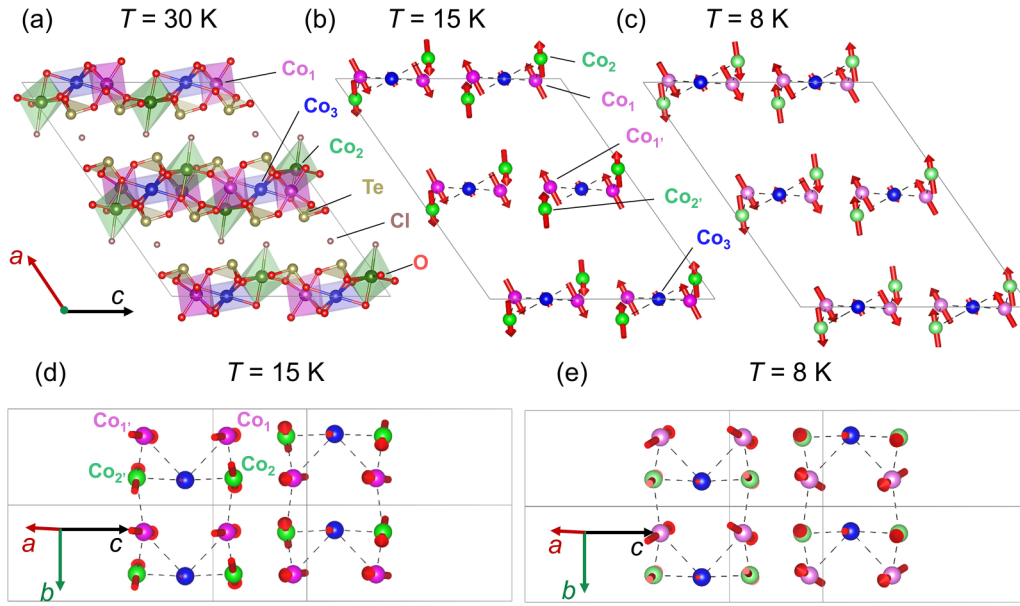


FIG. 4. (a) Illustrations of the crystal structure at 30 K. Schematic view of magnetic structures in the (b)  $ac$  projection and (d)  $bc$  projection at 15 K, and (c)  $ac$  projection and (e)  $bc$  projection at 8 K.

Interestingly, we clearly see a periodic variation of  $\Delta P$  upon rotating  $H$ , a direct proof of dominating linear ME effect in this system. In this configuration,  $H_{\perp} = H \sin \theta$  and  $H_{\parallel} = H \cos \theta$ , and  $\Delta P$  can be expressed as

$$\Delta P = H(\alpha_{\parallel} \cos \theta + \alpha_{\perp} \sin \theta) = H \sqrt{\alpha_{\perp}^2 + \alpha_{\parallel}^2} \sin(\theta + \theta_0), \quad (1)$$

where  $\theta_0 = \arctan(\alpha_{\parallel}/\alpha_{\perp})$ . In Fig. 7, we plot the electric polarization as a function of  $\theta$ , whereas a periodic variation of  $\Delta P$  can be observed. Here, the arrow indicates the direction of the scanning field (red arrow:  $0^{\circ} \sim 360^{\circ}$ , blue arrow:  $360^{\circ} \sim 0^{\circ}$ ). It is noted that the difference in the polarization value at  $\theta = 0^{\circ}$  and at  $\theta = 180^{\circ}$  may be due to the different preferred orientation distributions of the ceramic sample. We used sinusoidal function  $A^* \sin[(\theta - 66)\pi/180]$  as the green dashed line to fit  $\Delta P$ , and  $\theta_0 \approx 66^{\circ}$  can be deduced, giving rise to  $\alpha_{\parallel}/\alpha_{\perp} \approx 2.2$ . Intriguingly, this ratio is almost consistent

with our experimentally observed  $\alpha_{\parallel}/\alpha_{\perp} = 45/18 \approx 2.4$  from the data in Fig. 6.

### E. Magnetic property and ME effect in $\text{Co}_5(\text{TeO}_3)_4\text{Cl}_2$ single crystal

In order to clarify whether the measured ME anisotropy is solely due to the crystallographic orientation of the “grains” or its intrinsic property, further in-depth discussion regarding the ME effect and spin reorientation demonstrated in polycrystalline sample is highly needed. We were fortunate to obtain a small amount of  $\text{Co}_5(\text{TeO}_3)_4\text{Cl}_2$  single crystals, and to try and gather more information on the characteristics of spin reorientation through magnetization measurements. As shown in Fig. 8, the naturally grown crystals exhibit transparent and purple flaky morphology with the size of  $2 \times 3 \text{ mm}^2$ . We performed the room-temperature slow-scan XRD onto the naturally developed plane, and sharp peaks could be well indexed by the  $(h00)$  reflections. A narrow full width at half maximum (FWHM =  $0.04^{\circ}$ ) of the typical (200) orientation

TABLE II. Refined structural parameters and magnetic moments obtained from the NPD data taken at  $T = 15$  and 8 K. GOF stands for Goodness of fitting.

Temperature	Atom	Site	$m_x$ ( $\mu_B$ )	$m_y$ ( $\mu_B$ )	$M_z$ ( $\mu_B$ )	$m_{\text{tot}}$ ( $\mu_B$ )
15 K	Co1	8f	1.792 1	0.0912	0.2530	1.8122
	Co1'	8f	1.792 1	-0.0912	0.2530	1.8122
	Co2	8f	-1.819 9	0.8392	-0.9069	2.1997
	Co2'	8f	-1.821 99	-0.8392	-0.9069	2.1997
	Co3	4e	0.732 96	0	0.0613	0.7355
8 K	Co1	8f	2.792 0	-0.8026	0.3022	2.9207
	Co1'	8f	2.792 0	0.8026	0.3022	2.9207
	Co2	8f	-3.128 6	0.4152	-1.4235	3.4622
	Co2'	8f	-3.128 6	-0.4152	-1.4235	3.4622
	Co3	4e	1.297 7	0	0.1082	1.3022

$R_{\text{WP}} = 6.136$ , GOF = 5.79 at 8 K,  $R_{\text{WP}} = 5.242$ , GOF = 4.92 at 15 K.

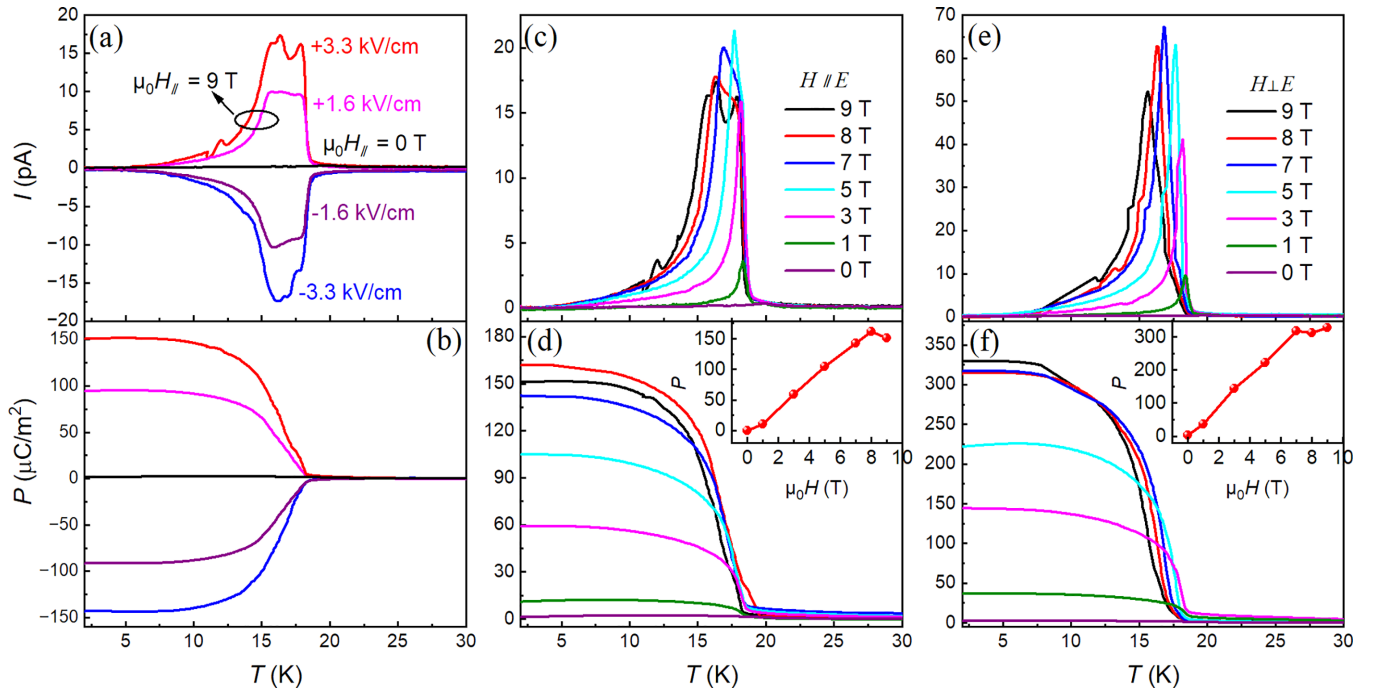


FIG. 5. (a) The pyroelectric current and (b) the electric polarization as a function of temperature collected at  $\mu_0 H_{\parallel} = 9$  T under different poling electric field. The black line shows the measured data at absence of magnetic field. (c) The pyroelectric current and (d) the electric polarization as a function of temperature under different magnetic fields in the  $H \parallel E$  configuration. The inset shows the  $H$ -dependent polarization at 2 K. (e) The pyroelectric current and (f) the electric polarization with the magnetic field perpendicular to the electric field. Inset: polarization curves with magnetic field at 2 K.

was found, indicative of strict orientation growth and high crystallinity. These high-quality single crystals offer the potential to conduct further detailed measurements. Figure 9(a) depicts the  $T$  dependence of magnetic susceptibility ( $\chi$ ) in the ZFC condition along the  $a^*$ ,  $b$ , and  $c$  axes, where  $a^* \perp bc$  plane.

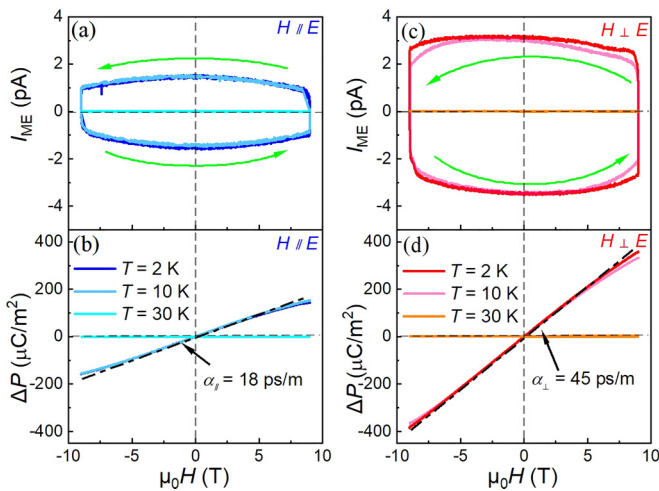


FIG. 6. The ME current  $I_{\text{ME}}$  as a function of  $H$  with (a)  $H \parallel E$  and (c)  $H \perp E$  measured at  $T = 2, 10$ , and  $30$  K, respectively. The green arrow indicates the direction of the scanning field. The magnetic field-dependent polarization  $\Delta P$  in the (b)  $H \parallel E$  and (d)  $H \perp E$  configuration measured at  $T = 2, 10$ , and  $30$  K, respectively. The black dashed-dotted lines in (b) and (d) serve as guides to the eye, indicating the linear relationship.

Upon further decreasing  $T$ , a broad peak appears at  $T_N \sim 18$  K which is assigned as antiferromagnetic Néel point, followed by a clear anomaly at  $T_S \sim 13$  K both along the  $a^*$  axis and  $b$  axis, indicating that rearrangements of magnetic moment may occur below  $T_S$ . As shown in Fig. 9(b), the Curie-Weiss fitting of the data from 100 to 300 K gives rise to the Curie-Weiss temperature  $\theta_{a^*} \sim -61$  K,  $\theta_b \sim -43$  K, and  $\theta_c \sim -73$  K (details are listed in Table IV), respectively, indicating the AFM nature of the  $\text{Co}^{2+}$  spin exchange and magnetic anisotropy. The derived effective paramagnetic moment along the  $a^*$  axis,  $b$  axis, and  $c$  axis is  $\mu_{\text{eff}} \sim 4.7 \mu_{\text{B}}/\text{Co}^{2+}$ ,  $5.0 \mu_{\text{B}}/\text{Co}^{2+}$ , and  $5.4 \mu_{\text{B}}/\text{Co}^{2+}$ , respectively, which falls in the expected spin-only moment  $3.87 \mu_{\text{B}}/\text{Co}$  and total effective moment  $6.64 \mu_{\text{B}}/\text{Co}$ , revealing the contribution from the orbital angular momentum via the spin-orbit coupling.

As shown in Fig. 9(c), the temperature dependence of pyroelectric current ( $I$ ) along the  $a^*$  axis reveals a notable anomaly at  $T_N$  when an applied magnetic field is aligned parallel to the  $b$  axis. The pyroelectric current and electric polarization under different  $H$  parallel to the  $b$  axis indicates magnetoelectric coupling, as shown in Figs. 9(c) and 9(d). The electric polarization  $P$  can be as large as  $\sim 170 \mu\text{C}/\text{m}^2$  at  $H_b = 9$  T and  $T = 2$  K, and the corresponding ME coefficient  $a_{xy} = 18$  ps/m. Here, we employ the Institute of Electrical and Electronic Engineers (IEEE) standard setting, where we define the physical property axis ( $x, y, z$ ), namely  $x \perp yz$  plane,  $y \parallel [010]$ , and  $z \parallel [001]$ . However, there are almost zero values in other magnetic directions,  $\alpha_{xx} = \alpha_{xz} = 0$ , which is consistent with the matrix form of the ME tensor for the  $C2'/c$  magnetic space group. Imposed by the magnetic point group  $2'/m$ , in principle there are four nonzero terms of ME coupling tensor:  $a_{xy}, a_{yx}$ ,

TABLE III. The ME performance of experimentally observed van der Waals ME materials.

Material	Spontaneous $P$ ( $\mu\text{C}/\text{m}^2$ )	Max $P$ ( $\mu\text{C}/\text{m}^2$ )	ME coefficients $\alpha$ (ps/m)	$T_{\text{FE}}$ (K)	Reference
MnI <sub>2</sub>	~80	~140 ( $\mu_0 H = 2$ T)	~30	3.9	[39]
CoI <sub>2</sub>	~8	~10 ( $\mu_0 H = 2$ T)	<1	10	[40]
NiI <sub>2</sub>	~50	~120 ( $\mu_0 H = 14$ T)	~20	58	[40]
NiBr <sub>2</sub>	~20	~25 ( $\mu_0 H = 2$ T)	<1	23	[41]
CuCl <sub>2</sub>	~25	~25 ( $\mu_0 H = 4$ T)	<1	24	[42]
CuBr <sub>2</sub>	~8	~22 ( $\mu_0 H = 9$ T)	~2	73	[43]
CuCrP <sub>2</sub> S <sub>6</sub>	0	<1	<1	32	[19]
FeTe <sub>2</sub> O <sub>5</sub> Cl	~3			11	[26]
Co <sub>5</sub> (TeO <sub>3</sub> ) <sub>4</sub> Cl <sub>2</sub>	0	~320 ( $\mu_0 H = 9$ T)	~45	18	This work

$a_{zy}$ , and  $a_{yz}$ . It is worth noting that due to the thin flakelike nature of the crystal along the  $a^*$  axis, it is not feasible to validate the magnetoelectric coupling coefficient in alternative directions. However, at the very least, the single-crystal data can demonstrate nondiagonal magnetoelectric coupling. Generally, the polarization of a polycrystalline sample is smaller compared to that of a single crystal. However, the polarization in this case is larger than that of a single crystal, indicating that polarization along other directions, such as the  $y$ - and  $z$ -axes polarization, might have larger values.

### F. Discussion

Co<sub>5</sub>(TeO<sub>3</sub>)<sub>4</sub>Cl<sub>2</sub> has a layered crystal structure that is stacked along the  $a$  axis by vdW force. According to the NPD analysis, one unit cell contains four clamplike cobalt pentamer cluster of [Co<sub>5</sub>O<sub>17</sub>Cl<sub>2</sub>], which consists of three inequivalent Co<sup>2+</sup> sites, named as Co<sub>1</sub>, Co<sub>1'</sub>, Co<sub>2</sub>, Co<sub>2'</sub>, Co<sub>3</sub>, and Co<sub>3'</sub> (Co<sub>1</sub> and Co<sub>1'</sub>, Co<sub>2</sub> and Co<sub>2'</sub> are related by inversion symmetry). The combination of magnetic anomaly at  $T_S \sim 13$  K and distinct temperature dependence of the nonequivalent Co sites demonstrates that rearrangements of magnetic moment may occur below  $T_S$ . However, the neutron scattering shows that magnetic space group  $C2'/c$  remains unchanged up to 8 K. As

a result, there are no anomalies in the temperature-dependent pyroelectric current and polarization curves before and after the spin reorientation.

According to the symmetry analysis, the magnetic point group  $2'/m$  forbids spontaneous polarization but allows linear ME effect. Here,  $2'$  is twofold rotation along the  $y$  direction, and  $m$  is a mirror perpendicular to the  $y$  axis. Meanwhile, due to the hidden symmetry  $-1'$ , Co<sub>5</sub>(TeO<sub>3</sub>)<sub>4</sub>Cl<sub>2</sub> does not exhibit macroscopic polarization. However, under an applied magnetic field, the breaking of  $2'$  or  $m$  symmetry allows for the occurrence of electric polarization. Our ME data for the single crystals provide clear evidence of the anisotropic ME coupling, which is consistent with the matrix form of the ME tensor. In linear magnetoelectric materials, the induced electric polarization (magnetization) is linearly proportional to the applied magnetic field (electric field) as expressed by  $P_i = \alpha_{ij}H_j$  or  $M_i = \alpha_{ji}E_j$ , where  $\alpha_{ij}$  is the first-order magnetoelectric coefficient. Typical linear magnetoelectric coupling materials, such as Cr<sub>2</sub>O<sub>3</sub> [42] and Co<sub>4</sub>Nb<sub>2</sub>O<sub>9</sub> [30], exhibit the fascinating properties of magnetically controlled polarization and electrically controlled magnetism. Based on the symmetry analysis using the tools at Bilbao Crystallographic Server [34], the magnetic point group  $2'/m$  also allows for four nonzero magnetoelectric tensor  $a_{xy}$ ,  $a_{yx}$ ,  $a_{zy}$ , and  $a_{yz}$ , which

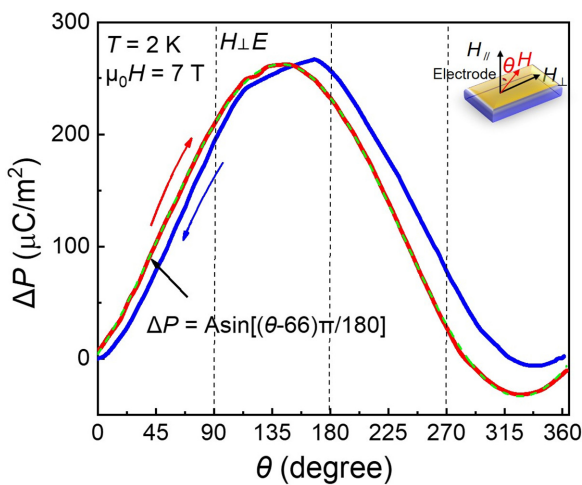


FIG. 7. Angular dependence of polarization under the rotating  $\Delta\mu_0 H = 7$  T at  $T = 2$  K. The arrow indicates the direction of the scanning field (red arrow:  $0^\circ \sim 360^\circ$ , blue arrow:  $360^\circ \sim 0^\circ$ ). Schematic sample configuration is shown in the upper right corner.

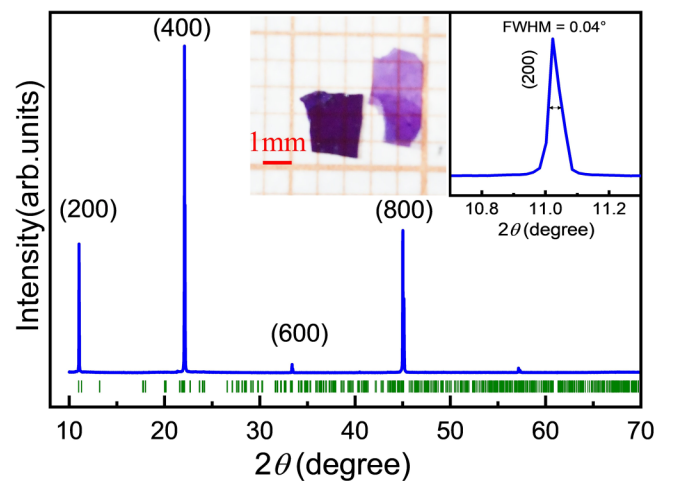


FIG. 8. The XRD pattern of the naturally grown large-scale plane of Co<sub>5</sub>(TeO<sub>3</sub>)<sub>4</sub>Cl<sub>2</sub> single crystal. Inset shows an optical image of a typical bulk crystal and the full width at half maximum (FWHM) of the (200) diffraction peak.



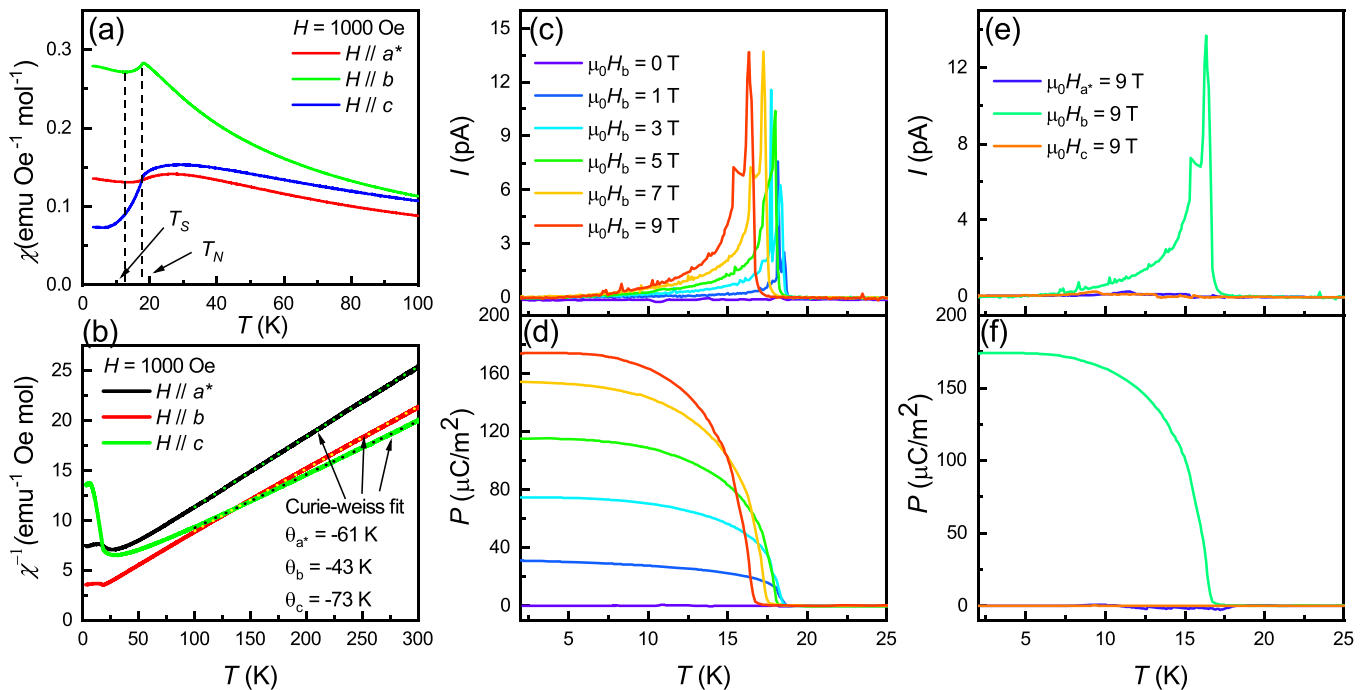


FIG. 9. (a) The  $T$  dependence of the magnetic susceptibility of  $\text{Co}_5(\text{TeO}_3)_4\text{Cl}_2$  single crystal under ZFC mode with measuring field  $\mu_0 H = 1$  kOe along the different crystallographic axes. (b) The  $T$ -dependent inverse susceptibility and the Curie-Weiss fitting of the data from 100 to 300 K. (c) The pyroelectric current ( $I$ ) and (d) the electric polarization ( $P$ ) as a function of temperature collected under different magnetic fields  $H//b$  axis. (e) The pyroelectric current and (f) the electric polarization as a function of temperature collected for  $H$  under different directions with  $\mu_0 H = 9$  T.

relates electric field with magnetization. In principle, there is significant potential for magnetism to be controlled by electrical means in  $\text{Co}_5(\text{TeO}_3)_4\text{Cl}_2$ . However, it is unfortunately not accessible at this moment, but deserves further investigation. The major difficulty lies in that the magnetization variation is expected to be very small and hard to detect, while the sample in the SQUID chamber must be connected with a stage which can be electrically controlled: it is challenging for a bulk single crystal.

Now, we turn to briefly discuss the magnetically induced polarization from a microscopic perspective. There are three well-known mechanisms to explain the microscopic origin of spin-driven ferroelectricity. In the exchange-striction mechanism, the electric polarization arises due to the symmetric exchange interaction. A prominent example of this is  $\text{Ca}_3\text{CoMnO}_6$ , which exhibits up-up-down-down collinear spin order [43]. On the contrary, the inverse Dzyaloshinskii-Moriya interaction or the spin current model is derived

from the antisymmetric exchange interaction in noncollinear magnetic orders, such as cycloidal or transverse conical spin structures [42]. The metal-ligand hybridization  $p-d$  mechanism gives the local electric polarization through the spin-orbit interaction in some low-symmetry system [44]. As shown in Fig. 4, The  $\text{Co}^{2+}$  magnetic moments form a noncoplanar magnetic structure, where the moments are almost entirely confined to the  $xz$  plane, forming a cycloid with the scalar product of neighboring magnetic moments as  $h = S_i \times S_j$  along the  $y$  direction. Then, a local electric polarization  $P_z$  (or  $P_x$ ) =  $h \times q$  along the  $z$  (or  $x$ ) direction can be established, in which  $q$  is the magnetic modulation vector along the  $x$  (or  $z$ ) axis. On the other hand, it is worth reminding that in a clamplike cobalt pentamer cluster of  $[\text{Co}_5\text{O}_{17}\text{Cl}_2]$ ,  $[\text{Co}(1)\text{O}_6]$ ,  $[\text{Co}(2)\text{O}_5\text{Cl}]$ , and  $[\text{Co}(3)\text{O}_6]$  octahedra exhibit low symmetry and significant distortion, which may also give rise to a local polarization due to the  $p-d$  hybridization mechanism. Hence, further measurements in the single crystal and theoretical calculation would be highly required to elucidate the contribution of ME coupling mechanisms in  $\text{Co}_5(\text{TeO}_3)_4\text{Cl}_2$ .

#### IV. CONCLUSION

To summarize, we have investigated the magnetic structure and anisotropic magnetoelectric coupling effects in the polycrystalline  $\text{Co}_5(\text{TeO}_3)_4\text{Cl}_2$  by combining magnetic susceptibility, heat capacity, neutron-powder diffraction, and electric polarization measurements. Unlike the Ni-based compounds, the magnetic order in  $\text{Co}_5(\text{TeO}_3)_4\text{Cl}_2$  is found to be noncoplanar with the moments preferentially pointing along the  $c$  axis. Furthermore,  $\text{Co}_5(\text{TeO}_3)_4\text{Cl}_2$  is characterized

TABLE IV. The Curie-Weiss temperature ( $\theta_{\text{CW}}$ ), frustration factor ( $f$ ), and effective moment ( $\mu_{\text{eff}}$ ) for  $\text{Co}_5(\text{TeO}_3)_4\text{Cl}_2$  in the geometry aligned parallel to  $a^*$  axis,  $b$  axis,  $c$  axis, and polycrystal, respectively.

$\text{Co}_5(\text{TeO}_3)_4\text{Cl}_2$	$T_N$ (K)	$\theta_{\text{CW}}$ (K)	$f$	$\mu_{\text{eff}}$ ( $\mu_B$ )
$a^*$	18	-61	3.4	4.7
$b$	18	-43	2.3	5.0
$c$	18	-73	4.1	5.4
Polycrystal	18	-68	3.8	5.2

by a significantly larger ferroelectric polarization and a more pronounced linear magnetoelectric coupling effect, compared to the van der Waals layered materials that have been discovered so far. The magnetically induced electric polarization is confirmed by the  $C2'/c$  magnetic space group determined by neutron scattering. In addition, we found that the electric polarization also exhibited periodical retention under a rotation of the magnetic field, and the fitted ratio of linear ME coefficient  $a_{\parallel}/\alpha_{\perp}$  is quite consistent with our experimental results. It is believed that the intriguing ME response to rotating magnetic field can be attributed to the continuous changes of antiferromagnetic moments. The establishment of  $\text{Co}_5(\text{TeO}_3)_4\text{Cl}_2$  as a member of the

two-dimensional layered magnetoelectric coupling family provides insights into designing the significant ME coupling properties in other van der Waals layered magnet.

#### ACKNOWLEDGMENTS

The authors would like to acknowledge the financial support from the National Natural Science Foundation of China (Grants No. 92163210, No. 12274231, No. 12074111, No. 52272108, No. 12304124, and No. 12304119). A portion of this research used resources at the Spallation Neutron Source, a DOE Office of Science User Facility operated by the Oak Ridge National Laboratory.

- [1] R. Ramesh and N. A. Spaldin, Multiferroics: Progress and prospects in thin films, *Nat. Mater.* **6**, 21 (2007).
- [2] W. Eerenstein, N. D. Mathur, and J. F. Scott, Multiferroic and magnetoelectric materials, *Nature (London)* **442**, 759 (2006).
- [3] M. Fiebig, Revival of the magnetoelectric effect, *J. Phys. D: Appl. Phys.* **38**, R123 (2005).
- [4] S. H. Baek, H. W. Jang, C. M. Folkman, Y. L. Li, B. Winchester, J. X. Zhang, Q. He, Y. H. Chu, C. T. Nelson, M. S. Rzechowski, X. Q. Pan, R. Ramesh, L. Q. Chen, and C. B. Eom, Ferroelastic switching for nanoscale non-volatile magnetoelectric devices, *Nat. Mater.* **9**, 309 (2010).
- [5] F. Matsukura, Y. Tokura, and H. Ohno, Control of magnetism by electric fields, *Nat. Nanotechnol.* **10**, 209 (2015).
- [6] V. Kocsis, T. Nakajima, M. Matsuda, A. Kikkawa, Y. Kaneko, J. Takashima, K. Kakurai, T. Arima, F. Kagawa, Y. Tokunaga, Y. Tokura, and Y. Taguchi, Magnetization-polarization cross-control near room temperature in hexaferrite single crystals, *Nat. Commun.* **10**, 1247 (2019).
- [7] I. A. Sergienko, C. Şen, and E. Dagotto, Ferroelectricity in the magnetic  $E$ -phase of orthorhombic perovskites, *Phys. Rev. Lett.* **97**, 227204 (2006).
- [8] Y. Tokura, S. Seki, and N. Nagaosa, Multiferroics of spin origin, *Rep. Prog. Phys.* **77**, 076501 (2014).
- [9] H. Wiegmann, A. G. M. Jansen, P. Wyder, J. P. Rivera, and H. Schmid, Magnetoelectric effect of  $\text{Cr}_2\text{O}_3$  in strong static magnetic fields, *Ferroelectrics* **162**, 141 (1994).
- [10] M. Pi, X. Xu, M. He, and Y. Chai, Microscopic origin of the spin-induced linear and quadratic magnetoelectric effects, *Phys. Rev. B* **105**, L020407 (2022).
- [11] K. Du, X. Xu, C. Won, K. Wang, S. A. Crooker, S. Rangan, R. Bartynski, and S.-W. Cheong, Topological surface magnetism and Néel vector control in a magnetoelectric antiferromagnet, *npj Quantum Mater.* **8**, 17 (2023).
- [12] J. P. Rivera, On definitions, units, measurements, tensor forms of the linear magnetoelectric effect and on a new dynamic method applied to Cr-Cl boracite, *Ferroelectrics* **161**, 165 (1994).
- [13] S.-W. Cheong, SOS: Symmetry-operational similarity *npj Quantum Mater.* **4**, 53 (2019).
- [14] F. Liu, L. You, K. L. Seyler, X. Li, P. Yu, J. Lin, X. Wang, J. Zhou, H. Wang, H. He, S. T. Pantelides, W. Zhou, P. Sharma, X. Xu, P. M. Ajayan, J. Wang, and Z. Liu, Room-temperature ferroelectricity in  $\text{CuInP}_2\text{S}_6$  ultrathin flakes, *Nat. Commun.* **7**, 12357 (2016).
- [15] W. Ding, J. Zhu, Z. Wang, Y. Gao, D. Xiao, Y. Gu, Z. Zhang, and W. Zhu, Prediction of intrinsic two-dimensional ferroelectrics in  $\text{In}_2\text{Se}_3$  and other III<sub>2</sub>-VI<sub>3</sub> van der Waals materials, *Nat. Commun.* **8**, 14956 (2017).
- [16] Y. Zhou, D. Wu, Y. Zhu, Y. Cho, Q. He, X. Yang, K. Herrera, Z. Chu, Y. Han, M. C. Downer, H. Peng, and K. Lai, Out-of-plane piezoelectricity and ferroelectricity in layered  $\alpha$ - $\text{In}_2\text{Se}_3$  nanoflakes, *Nano Lett.* **17**, 5508 (2017).
- [17] C. Gong, L. Li, Z. Li, H. Ji, A. Stern, Y. Xia, T. Cao, W. Bao, C. Wang, Y. Wang, Z. Q. Qiu, R. J. Cava, S. G. Louie, J. Xia, and X. Zhang, Discovery of intrinsic ferromagnetism in two-dimensional van der Waals crystals, *Nature (London)* **546**, 265 (2017).
- [18] B. Huang, G. Clark, E. Navarro-Moratalla, D. R. Klein, R. Cheng, K. L. Seyler, D. Zhong, E. Schmidgall, M. A. McGuire, D. H. Cobden, W. Yao, D. Xiao, P. Jarillo-Herrero, and X. D. Xu, Layer-dependent ferromagnetism in a van der Waals crystal down to the monolayer limit, *Nature (London)* **546**, 270 (2017).
- [19] G. Qiu, Z. Li, K. Zhou, and Y. Cai, Flexomagnetic noncollinear state with a plumb line shape spin configuration in edged two-dimensional magnetic  $\text{CrI}_3$ , *npj Quantum Mater.* **8**, 15 (2023).
- [20] C. B. Park, A. Shahee, K. T. Kim, D. R. Patil, S. A. Guda, N. Ter-Oganessian, and K. H. Kim, Observation of spin-induced ferroelectricity in a layered van der Waals antiferromagnet  $\text{CuCrP}_2\text{S}_6$ , *Adv. Electron. Mater.* **8**, 2101072 (2022).
- [21] X. Wang, Z. Shang, C. Zhang, J. Kang, T. Liu, X. Wang, S. Chen, H. Liu, W. Tang, Y.-J. Zeng, J. Guo, Z. Cheng, L. Liu, D. Pan, S. Tong, B. Wu, Y. Xie, G. Wang, J. Deng, T. Zhai, H.-X. Deng, J. Hong, and J. Zhao, Electrical and magnetic anisotropies in van der Waals multiferroic  $\text{CuCrP}_2\text{S}_6$ , *Nat. Commun.* **14**, 840 (2023).
- [22] Y. Lai, Z. Song, Y. Wan, M. Xue, C. Wang, Y. Ye, L. Dai, Z. Zhang, W. Yang, H. Du, and J. Yang, Two-dimensional ferromagnetism and driven ferroelectricity in van der Waals  $\text{CuCrP}_2\text{S}_6$ , *Nanoscale* **11**, 5163 (2019).
- [23] Q. Song, C. A. Occhialini, E. Ergecen, B. Ilyas, D. Amoroso, P. Barone, J. Kapeghian, K. Watanabe, T. Taniguchi, A. S. Botana, S. Picozzi, N. Gedik, and R. Comin, Evidence for a single-layer van der Waals multiferroic, *Nature (London)* **602**, 601 (2022).
- [24] S. Son, Y. Lee, J. H. Kim, B. H. Kim, C. Kim, W. Na, H. Ju, S. Park, A. Nag, K. J. Zhou, Y. W. Son, H. Kim, W. S.

- Noh, J. H. Park, J. S. Lee, H. Cheong, J. H. Kim, and J. G. Park, Multiferroic-enabled magnetic-excitons in 2D quantum-entangled van der Waals antiferromagnet  $\text{NiI}_2$ , *Adv. Mater.* **34**, e2109144 (2022).
- [25] H. Ju, Y. Lee, K. T. Kim, I. H. Choi, C. J. Roh, S. Son, P. Park, J. H. Kim, T. S. Jung, J. H. Kim, K. H. Kim, J. G. Park, and J. S. Lee, Possible persistence of multiferroic order down to bilayer limit of van der Waals material  $\text{NiI}_2$ , *Nano Lett.* **21**, 5126 (2021).
- [26] Y. Jiang, Y. Wu, J. Zhang, J. Wei, B. Peng, and C.-W. Qiu, Dilemma in optical identification of single-layer multiferroics, *Nature* **619**, E40 (2023).
- [27] M. Johnsson, K. W. Törnroos, P. Lemmens, and P. Millet, crystal structure and magnetic properties of a new two-dimensional  $S = 1$  quantum spin system  $\text{Ni}_5(\text{TeO}_3)_4\text{X}_2$  ( $\text{X} = \text{Cl}, \text{Br}$ ), *Chem. Mater.* **15**, 68 (2003).
- [28] R. Becker, M. Prester, H. Berger, M. Johnsson, D. Drobac, and I. Zivkovic, Crystal structure and magnetic properties of the new cobalt tellurite halide  $\text{Co}_5(\text{TeO}_3)_4\text{X}_2$  ( $\text{X} = \text{Cl}, \text{Br}$ ), *Solid State Sci.* **9**, 223 (2007).
- [29] M. Pregelj, A. Zorko, H. Berger, H. van Tol, L. C. Brunel, A. Ozarowski, S. Nellutla, Z. Jagličič, O. Zaharko, P. Tregenna-Piggott, and D. Arčon, Magnetic structure of the  $S = 1$   $\text{Ni}_5(\text{TeO}_3)_4\text{Br}_2$  layered system governed by magnetic anisotropy, *Phys. Rev. B* **76**, 144408 (2007).
- [30] L. H. Yin, Y. M. Zou, J. Yang, J. M. Dai, W. H. Song, X. B. Zhu, and Y. P. Sun, Colossal magnetodielectric effect and spin flop in magnetoelectric  $\text{Co}_4\text{Nb}_2\text{O}_9$  crystal, *Appl. Phys. Lett.* **109**, 032905 (2016).
- [31] I. V. Solovyev and T. V. Kolodiazhnyi, Origin of magnetoelectric effect in  $\text{Co}_4\text{Nb}_2\text{O}_9$  and  $\text{Co}_4\text{Ta}_2\text{O}_9$ : The lessons learned from the comparison of first-principles-based theoretical models and experimental data, *Phys. Rev. B* **94**, 094427 (2016).
- [32] A. Maignan and C. Martin,  $\text{Fe}_4\text{Nb}_2\text{O}_9$ : A magnetoelectric antiferromagnet, *Phys. Rev. B* **97**, 161106(R) (2018).
- [33] B. H. Toby and R. B. Von Dreele, GSAS-II: The genesis of a modern open-source all purpose crystallography software package, *J. Appl. Crystallogr.* **46**, 544 (2013).
- [34] J. M. Perez-Mato, S. V. Gallego, E. S. Tasci, L. Elcoro, G. de la Flor, and M. I. Aroyo, Symmetry-based computational tools for magnetic crystallography, *Annu. Rev. Mater. Sci.* **45**, 217 (2015).
- [35] L. J. Vera Stimpson, E. E. Rodriguez, C. M. Brown, G. B. G. Stenning, M. Jura, and D. C. Arnold, Magnetic ordering in a frustrated bow-tie lattice, *J. Mater. Chem. C* **6**, 4541 (2018).
- [36] V. O. Garlea, M. A. McGuire, L. D. Sanjeeva, D. M. Pajerowski, F. Ye, and J. W. Kolis, The magnetic order of a manganese vanadate system with two-dimensional striped triangular lattice, *AIP Adv.* **8**, 101407 (2018).
- [37] T. Kurumaji, S. Seki, S. Ishiwata, H. Murakawa, Y. Tokunaga, Y. Kaneko, and Y. Tokura, Magnetic-field induced competition of two multiferroic orders in a triangular-lattice helimagnet  $\text{MnI}_2$ , *Phys. Rev. Lett.* **106**, 167206 (2011).
- [38] T. Kurumaji, S. Seki, S. Ishiwata, H. Murakawa, Y. Kaneko, and Y. Tokura, Magnetoelectric responses induced by domain rearrangement and spin structural change in triangular-lattice helimagnets  $\text{NiI}_2$  and  $\text{CoI}_2$ , *Phys. Rev. B* **87**, 014429 (2013).
- [39] Y. Tokunaga, D. Okuyama, T. Kurumaji, T. Arima, H. Nakao, Y. Murakami, Y. Taguchi, and Y. Tokura, Multiferroicity in  $\text{NiBr}_2$  with long-wavelength cycloidal spin structure on a triangular lattice, *Phys. Rev. B* **84**, 060406(R) (2011).
- [40] S. Seki, T. Kurumaji, S. Ishiwata, H. Matsui, H. Murakawa, Y. Tokunaga, Y. Kaneko, T. Hasegawa, and Y. Tokura, Cupric chloride  $\text{CuCl}_2$  as an  $S = 1/2$  chain multiferroic, *Phys. Rev. B* **82**, 064424 (2010).
- [41] L. Zhao, T. L. Hung, C. C. Li, Y. Y. Chen, M. K. Wu, R. K. Kremer, M. G. Banks, A. Simon, M. H. Whangbo, C. Lee, J. S. Kim, I. Kim, and K. H. Kim,  $\text{CuBr}_2$  – a new multiferroic material with high critical temperature, *Adv. Mater.* **24**, 2469 (2012).
- [42] A. Iyama and T. Kimura, Magnetoelectric hysteresis loops in  $\text{Cr}_2\text{O}_3$  at room temperature, *Phys. Rev. B* **87**, 180408(R) (2013).
- [43] Y. J. Choi, H. T. Yi, S. Lee, Q. Huang, V. Kiryukhin, and S. W. Cheong, Ferroelectricity in an Ising chain magnet, *Phys. Rev. Lett.* **100**, 047601 (2008).
- [44] T.-h. Arima, Ferroelectricity induced by proper-screw type magnetic order, *J. Phys. Soc. Jpn.* **76**, 073702 (2007).